

MLO: Multi-Object Tracking and Lidar Odometry in Dynamic Environment

Tingchen Ma and Yongsheng Ou*

Abstract—The SLAM system built on the static scene assumption will introduce significant estimation errors when a large number of moving objects appear in the field of view. Tracking and maintaining semantic objects is beneficial to understand the scene and provide rich decision information for planning and control modules. This paper introduces MLO, a multi-object Lidar odometry which tracks ego-motion and movable objects with only the lidar sensor. First, it achieves information extraction of foreground movable objects, surface road, and static background features based on geometry and object fusion perception module. While robustly estimating ego-motion, Multi-object tracking is accomplished through the least-squares method fused by 3D bounding boxes and geometric point clouds. Then, a continuous 4D semantic object map on the timeline can be created. Our approach is evaluated qualitatively and quantitatively under different scenarios on the public KITTI dataset. The experiment results show that the ego localization accuracy of MLO is better than A-LOAM system in highly dynamic, unstructured, and unknown semantic scenes. Meanwhile, the multi-object tracking method with semantic-geometry fusion also has apparent advantages in accuracy and tracking robustness compared with the single method.

Index Terms—Lidar SLAM, semantic map, multi-object tracking, dynamic scene

I. INTRODUCTION

Simultaneous localization and mapping is the problem of creating a map model and estimating ego localization during the motion of a robot equipped with specific sensors. In recent years, lidar SLAM has been widely used in industry due to its good scene robustness (illumination [22], low texture [24]). However, visual [21] or lidar [39] SLAM systems based on static rigidity assumption will introduce significant estimation errors when many moving objects are in the scene. Therefore, The processing method of dynamic objects will determine system performance in real-world applications, such as AR and driverless technology.

This work was supported by the National Key Research and Development Program of China under Grant 2018AAA0103001; in part by the National Natural Science Foundation of China (Grants No. U1813208, 62173319, 62063006); in part by the Guangdong Basic and Applied Basic Research Foundation (2020B1515120054); in part by the Shenzhen Fundamental Research Program (JCYJ20200109115610172).

* Corresponding author, e-mail: ys.ou@siat.ac.cn.

Tingchen Ma is with the Shenzhen Institute of Advanced Technology, Chinese Academy of Sciences, Shenzhen 518055, China, and also with the Shenzhen College of Advanced Technology, University of Chinese Academy of Sciences, Shenzhen 518055, China.

Yongsheng Ou is with the CAS Key Laboratory of Human-Machine-Intelligence Synergic Systems, Shenzhen Institute of Advanced Technology, Chinese Academy of Sciences, Shenzhen 518055, China, and also with the Guangdong Provincial Key Laboratory of Robotics and Intelligent System, Shenzhen Institute of Advanced Technology, Chinese Academy of Sciences, Shenzhen 518055, China

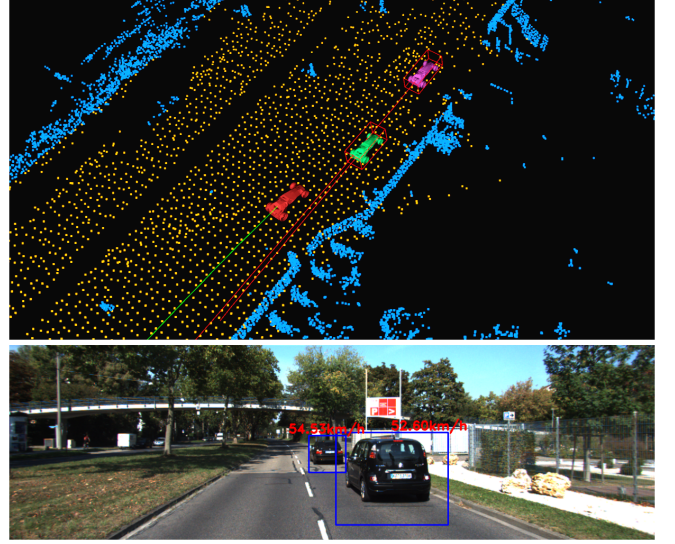


Fig. 1. Qualitative results for sequence 0926-0013 in KITTI-raw dataset. The upper part of picture is the display result in rviz. Red car is the robot equipped with Lidar, and green line segment is corresponding moving path. Red line segment is the continuous path of objects. The bottom half is the projected 2d bounding box (blue) and corresponding object velocity estimation (red) in the image with synchronized timestamp.

A relatively simple way to deal with dynamic objects is to treat them as outliers. By checking geometric consistency, motion constraints [37], or extracting semantic objects in a single frame using the powerful prior inference model [17], those parts that may affect system reliability can be eliminated [26]. However, it is dangerous to ignore this information in real and complex scenes, such as pedestrians and vehicles, which are also the core elements of planning and decision modules. So, these real needs also promote the development of simultaneous localization, mapping, and moving object tracking technology (SLAMMOT) [33].

Compared with point clouds, obtaining the same spatial point in different images is more intuitive. For example, [25], [40] used the feature descriptor or dense optical flow [30] to complete data association and build an object-aware semantic SLAM system. On the other hand, the point cloud acquired by 3D Lidar is discrete and non-repetitive, making it more difficult to obtain stable object data association and achieve accurate object state estimation.

In this paper, we propose a novel multi-object Lidar odometry framework, which aims to solve the problem of simultaneous localization, mapping, and multi-objects tracking using only a Lidar sensor. First, based on the multi-task fusion per-

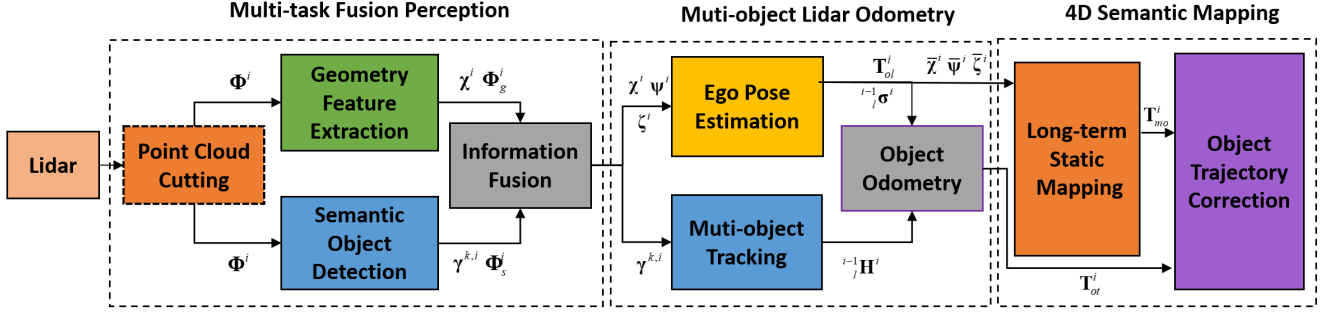


Fig. 2. **MLO system flow diagram.** MLO system can be divided into three modules: multi-task fusion perception, multi-object laser odometry and 4D semantic mapping. Solid-line boxes represent necessary modules, and dashed-line boxes represent optional modules.

ception module, motion-consistent object point clouds, static ground, and background features can be extracted reliably. Then, the ground features, background segment, and surface features filtered with a geometric consistency algorithm are used for ego localization and long-term consistency map construction. Meanwhile, a least-squares estimation method fused with 3D bounding boxes (3D-BB) and geometric point clouds is used to complete foreground movable objects tracking, and their motion states are also maintained in the map. Finally, we verify the accuracy and robustness of ego localization and multi-object tracking on the public KITTI [10] dataset.

II. RELATED WORK

Compared with the method of detection and rejection [4], [8], maintaining objects in the map has broader application scenarios. Achieving this goal requires tracking objects while detecting them.

[15], [34] proposed detection models for specific objects, such as pedestrians and vehicles, and completed tracking with a filter algorithm. [19] proposed a general object segmentation method based on the local convexity criterion. They used the Kalman filter [13] and ICP algorithm [5] for multi-object tracking. Assuming local geometric constancy and the regularization of smooth motion field, [7] estimated different object-motion through rigid scene flow. Specially, this method can fit non-rigid motions such as pedestrians. [35] used POINT-RCNN [28] to detect semantic objects in point clouds, then used the Kalman filter to track 3D-BB. [1] used a parallel mean shift algorithm to detect and localize objects in the 2D image and 3D point cloud. They achieved reliable object tracking through a 2D/3D fusion Kalman filter method.

[32] was the first paper to derive the Bayesian formula for localization, mapping, and moving object tracking, which laid the theoretical foundation for solving this problem. Their system used two extended Kalman filters to complete SLAM and multi-object tracking tasks. [6] used RANSAC [9] to sequentially estimate the motion model. Then point clouds were associated with corresponding models through a Bayesian approach. This method assumed that most information within the scene was static. [2] used GPS/IMU for ego localization and background subtraction to extract moving objects in octree voxel maps. Then it performed 3D-BB tracking by Kalman filter. [23] matched measurements to local spherical

coordinates and identified dynamic points based on a prior map. The transformation of each point was calculated using a non-rigid ICP algorithm, and the translational vector was extracted to calculate the velocity. [20] was an extension of [19], which simultaneously completed ego localization and multi-object tracking by treating the static background as an object. However, the author ignored the problem of mapping.

For visual SLAMMOT, [12] used RANSAC to track static background and moving objects separately. [11], [40] used the feature method or optical flow method for object tracking and jointly optimized ego poses, object trajectories, and landmarks through bundle adjustment [31] at the back-end, which improved the mapping accuracy of the system. In addition, [11] derived coordinate transformation formula of point features for the rigid moving object.

III. METHOD

MLO is built on popular LOAM [39] and includes three modules: multi-task fusion perception, multi-object Lidar odometry, and 4D semantic object mapping. For each input frame, motion-consistent object point clouds and static ground and background features are extracted by the fusion perception module. Then, ego pose estimation with motion consistency check and multi-object relative increment estimation are performed in parallel. Each object pose is calculated in odom coordinate. Finally, a long-term static map is constructed using both ground and background information. Meanwhile, the trajectory of each object in map coordinate can be corrected.

A. Notation and Coordinate Frames

In this paper, we define notation as follow: Lidar has a pose \mathbf{T}_{ol}^i at time i in odom coordinate. It can simultaneously observe static ground, background point cloud ${}^l\mathbf{x}_j \in \mathbb{R}^3$, and movable objects with pose \mathbf{T}_{ot}^i in odom coordinate. Each observed object contains 3d object points ${}^l\mathbf{x}_j^{k,i} \in \mathbb{R}^3$. At the same time, the Lidar pose in map coordinate is \mathbf{T}_{ml}^i , and the corresponding corrected pose of objects are $\mathbf{T}_{mt}^{k,i}$.

B. Multi-task Fusion Perception

After getting the ROI point cloud Φ^i of current Lidar frame, we perform geometric feature extraction and semantic object detection in parallel to obtain preliminary object point clouds

and geometric environment description. Then the information fusion module can receive more accurate object points segmentation and static environment features through a mutual correction step.

1) Geometric feature extraction. The geometric feature extraction module computes smoothness for subsequent background feature selection after completing ground feature extraction. Using the iterative PCA algorithm proposed in [38], ground fitting is achieved and the corresponding points are labeled in point cloud Φ_g^i .

Then, we calculate the distortion correction time and divide the scan line into segments. By segment-by-segment detection of the ground labels (**0**: background point, **1**: ground point) calculated above, the id pairs of the head and tail points in each segment are stored in the ground container \mathbf{V}_g and the background container \mathbf{V}_b .

Based on the smoothness calculation method proposed in [39], we can extract ground features χ_f^i from the point cloud in container \mathbf{V}_g . The average smoothness S_a of ground features is obtained as follows:

$$S_a = \sum_{o=1}^N c_o / N_c \quad (1)$$

where c_o is the smoothness of o -th ground feature, and N_c is the total number of ground features in current frame. S_a will be used for selecting practical background surface features. After downsampling all ground points, a candidate ground point cloud χ_c^i is generated.

For point clouds contained in \mathbf{V}_b , we only compute and sort the smoothness here. The fine selection of background features will be performed in the following information fusion module.

2) Semantic object detection. Semantic object detection module is to obtain 3D-BB and foreground object point clouds they enclose. For the motion estimation of the movable object, 3D-BB will be used to provide optimization constraints. We accomplish above tasks with 3DSSD [36], a one-stage, point-based, lightweight object detection model that balances detection accuracy and efficiency. The 3D-BB are represented as follows:

$$\tau^{k,i} = [x^{k,i}, y^{k,i}, z^{k,i}, l^{k,i}, w^{k,i}, h^{k,i}, yaw^{k,i}]^T \quad (2)$$

where (x, y, z) represents the object position, (l, w, h) represents the 3D-BB size and yaw is the direction angle of the object. Each group of object point cloud in 3D-BB is stored as $\gamma^{k,i}$. Then they are marked with independent object id in Φ_s^i . Their semantic confidences are denoted as $\mu^{k,i}$.

3) Information fusion. Considering that there is intersection information for ground features and object point clouds extracted during parallel detection, it is necessary to perform mutual correction first to ensure their motion consistency. According to the object id marked in Φ_s^i , object points in ground feature sets χ_f^i and χ_c^i are eliminated. Similarly, the ground feature in each object point cloud can be rejected by labels in Φ_g^i .

For point clouds contained in \mathbf{V}_b , which do not belong to semantic objects and ground features, we use their smoothness

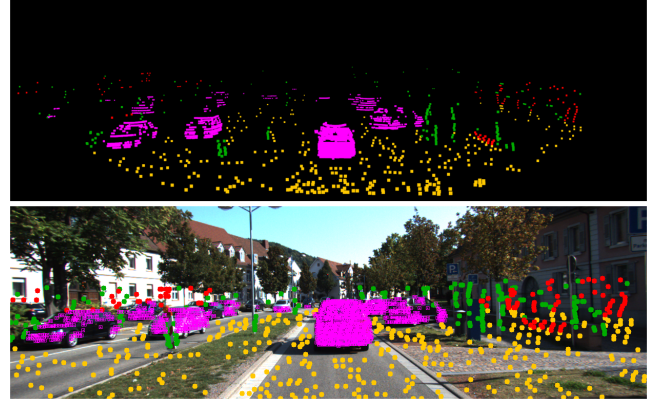


Fig. 3. The results of multi-task fusion perception module for sequence 0926-0056 in the KITTI-raw dataset. Pink point clouds represent moving cars, yellow point cloud is ground feature. Green and red point cloud are background segment and surface features, respectively.

to select background segment features ψ_f^i , surface features ζ_f^i , and corresponding candidate sets ψ_c^i, ζ_c^i .

C. Multi-object Lidar Odometry

Based on the perception results in Section B, the odometry module firstly estimates the absolute increment for ego-motion and relative motion increment for each semantic object in parallel. Then, each object pose is calculated in object-fixed coordinate [11].

1) Robust ego odometry. Before entering the ego-motion estimation process, **Algorithm 1** is used to achieve a geometric consistency check on the ground and background features, eliminating unknown dynamic influences that cannot be identified by the object detection module (section 3.2.2). The feature sets that passed the geometric consistency check are denoted as $(\tilde{\chi}_f^i, \tilde{\psi}_f^i, \tilde{\zeta}_f^i)$.

For improving the computational efficiency of ego odometry, we use the two-step algorithm proposed by [27] for pose estimation. Firstly, frame increment $[t_z, \theta_{roll}, \theta_{pitch}]$ is computed based on matching points in checked ground feature set $\tilde{\chi}_f^i$, and the distortion-corrected candidate feature set $\tilde{\chi}_c^{i-1}$. Then, the increment $[t_z, \theta_{roll}, \theta_{pitch}]$ is fixed, and another 3 degrees of freedom increment $[t_x, t_y, \theta_{yaw}]$ is estimated based on segment feature set $\tilde{\psi}_f^i$, surface features in $\tilde{\zeta}_f^i$ with more "flat" smoothness than S_a and their corresponding candidate sets. Finally, we obtain ego pose \mathbf{T}_{ol}^i at time i by accumulating the 6-DOF increment ${}^{i-1}_l \sigma^i$.

2) Multi-object tracking. The multi-object tracking module maintains a tracking list containing object information (object point cloud, sampling point on 3d-BB and pose in Lidar coordinate) and tracking state (optimization result evaluation tracking continuity evaluation) to achieve object data association and relative motion increment estimation.

First, we use the constant relative motion model to predict object position in current Lidar coordinate, which, together with object detection position, constitutes the position error term \mathbf{e}_l . Meanwhile, the direction error term \mathbf{e}_d is formed by the relative motion direction of the object, the 3D-BB size is used to calculate the scale error term \mathbf{e}_s and object point cloud

Algorithm 1: Geometric consistency feature check

Input: Current feature sets: $(\chi_f^i, \psi_f^i, \zeta_f^i)$, candidate sets without distortion: $(\bar{\chi}_c^{i-1}, \bar{\psi}_c^{i-1}, \bar{\zeta}_c^{i-1})$, increment ${}_l^{i-1}\sigma^i$ from last loop, association update interval λ , thresholds: (th_r, th_g, th_b)

Output: Consistent feature sets: $(\tilde{\chi}_f^i, \tilde{\psi}_f^i, \tilde{\zeta}_f^i)$
The number of feature sets $(\chi_f^i, \psi_f^i, \zeta_f^i)$ is recorded as N_f . Let ${}_l^{i-1}\sigma_{best}^i = {}_l^{i-1}\sigma^i$;

for $i = 1 : N_{iter}$ **do**

if $i \% \lambda = 0$ **then**

 Based on ${}_l^{i-1}\sigma_{best}^i$ and $(\chi_f^i, \psi_f^i, \zeta_f^i)$ including distortion correction time, feature position at the initial time of current frame is computed; Search their closest points in kd-trees formed by $(\bar{\chi}_c^{i-1}, \bar{\psi}_c^{i-1}, \bar{\zeta}_c^{i-1})$. Then correct $(\chi_f^i, \psi_f^i, \zeta_f^i)$ to the end of current frame, denoted as $(\mathbf{m}_{\chi_f}, \mathbf{m}_{\psi_f}, \mathbf{m}_{\zeta_f})$;

end

 Random select matching pairs from $\mathbf{m}_{\chi_f}, \mathbf{m}_{\psi_f}$ and their candidate sets;

 Update ${}_l^{i-1}\sigma^i$ with matching pairs and ICP model; Transform $(\chi_f^i, \psi_f^i, \zeta_f^i)$ to the initial time of current frame with ${}_l^{i-1}\sigma^i$. Find their closest points in kd-trees to perform Euclidean distance check;

 Record the number of points passing the check as $(\eta_{\chi_f}, \eta_{\psi_f}, \eta_{\zeta_f})$. Let $\eta_n = \eta_{\chi_f} + \eta_{\psi_f} + \eta_{\zeta_f}$;

if $((\eta_{\chi_f} + \eta_{\psi_f} + \eta_{\zeta_f})/N_f \geq th_r) \wedge (\eta_{\chi_f} \geq th_g) \wedge (\eta_{\psi_f} + \eta_{\zeta_f} \geq th_b) \wedge (\eta_n > \eta_{best})$ **then**

 Record feature sets $(\tilde{\chi}_f^i, \tilde{\psi}_f^i, \tilde{\zeta}_f^i)$;

 Let $\eta_{best} = \eta_{\chi_f} + \eta_{\psi_f} + \eta_{\zeta_f}$, ${}_l^{i-1}\sigma_{best}^i = {}_l^{i-1}\sigma^i$;

end

end

number is used to calculate the shape error term \mathbf{e}_n . Then, the association matrix is solved by Kuhn-Munkres algorithm to obtain the matching relationship of objects between frames. The calculation method of each error term can refer to [3].

To robustly and accurately compute relative motion increments of each object, this paper designs a least-squares estimation method that fuses both 3D-BB and geometric point clouds. First, we use the voxelized general ICP algorithm proposed in [14] to construct the cost function of object point cloud. At the same time, the constant relative motion model will be used for correcting the distortion caused by Lidar and object motion.

Assuming that in Lidar coordinate, the j -th point on current processing object is ${}_l^i\mathbf{x}_j^i$, and its corresponding timestamp is t_k . Let ${}_l^{i-1}\mathbf{H}_k^i$ denote pose transform between interval $[t^{i-1}, t_k]$. Then ${}_l^{i-1}\mathbf{H}_k^i$ can be calculated by linear interpolation of the relative motion increment ${}_l^{i-1}\mathbf{H}^i$:

$${}_l^{i-1}\mathbf{H}_k^i = \frac{t_k - t^i}{t^{i-1} - t^i} {}_l^{i-1}\mathbf{H}^i \quad (3)$$

The geometric error term $\mathbf{e}_{g,j}$ containing motion distortion correction is expressed as:

$$\mathbf{e}_{g,j} = \frac{\sum {}_l^i\mathbf{v}_m^{i-1}}{N_j} - {}_l^{i-1}\mathbf{H}_j^i {}_l^i\mathbf{x}_j^i \quad (4)$$

where ${}_l^i\mathbf{v}_m^{i-1}$ is the point in voxel matched at the end of last frame, N_j is the number of 3D points contained in the matched voxel. The calculation formula of the covariance matrix $\mathbf{\Omega}_j$ corresponding to the error term $\mathbf{e}_{g,j}$ is as follows:

$$\mathbf{\Omega}_j = \frac{\sum C_m^{i-1}}{N_j} - {}_l^{i-1}\mathbf{H}_j^i C_j^i {}_l^{i-1}\mathbf{H}_j^{iT} \quad (5)$$

C_m^{i-1} and C_j^i represent the variance of matched voxel and the corresponding voxel where ${}_l^i\mathbf{x}_j^i$ locates, respectively.

On the other hand, since objects detected in a single frame are local observation. Inevitably, the cost function formed by Eq. (4) sometimes cannot constrain the 6-DOF object motion. Therefore, we propose introducing semantic constraints to achieve the reliable increment estimation. By performing uniform sampling on each edge of 3D-BB τ^i , it is easy to obtain 3d points with direct matching relationships between frames. Then, the semantic error term $\mathbf{e}_{b,r}$ without motion distortion correction can be denoted as:

$$\mathbf{e}_{b,r} = {}_l^i\mathbf{y}_r^{i-1} - {}_l^{i-1}\mathbf{H}^i {}_l^i\mathbf{y}_r^i \quad (6)$$

where ${}_l^i\mathbf{y}_r^{i-1}$ is the corresponding 3d point on the 3D-BB of last frame. Finally, Eq. (7) is the cost function of relative motion estimation considering the semantic confidence:

$$\arg \min_{{}_l^{i-1}\mathbf{H}^i} \frac{2 - \mu^i}{2N_g} \sum_{j=1}^{N_g} (N_j \mathbf{e}_{g,j}^T \mathbf{\Omega}_j^{-1} \mathbf{e}_{g,j}) + \frac{\mu^i}{2N_b} \sum_{r=1}^{N_b} (\mathbf{e}_{b,r}^T \mathbf{e}_{b,r}) \quad (7)$$

N_g is the number of an object point cloud. When sample points on each edge are Λ , the corresponding number of sampling points on 3D-BB is $N_b = 12\Lambda - 4$.

In this paper, we use LM [16] algorithm to solve Eq. (7).

3) Object odometry. Based on calculation results of ego odometry (Section 3.3.1) and multi-object tracking module (Section 3.3.2), object pose in odom coordinate can be computed. First, object motion increment in Lidar coordinate is denoted as:

$${}_l^i\mathbf{X}^{i-1} = {}_l^{i-1}\sigma^i {}_l^i\mathbf{H}^{i-1} \quad (8)$$

Then, combined with the object-fixed coordinate proposed in [11] (as shown in Fig.4), and assuming that the transform matrix from object to Lidar at time $i-1$ is ${}_t^{i-1}\mathbf{L}_{lt}$, we can obtain absolute object motion increment ${}_t^{i-1}\mathbf{X}^i$ in object-fixed coordinate:

$${}_t^{i-1}\mathbf{X}^i = {}_t^{i-1}\mathbf{L}_{lt}^{-1} {}_l^i\mathbf{X}^{i-1} {}_l^{i-1}\mathbf{L}_{lt} \quad (9)$$

Odometry pose \mathbf{T}_{ot}^i for each object at time i can be computed by accumulating increments ${}_t^{i-1}\mathbf{X}^i$. In this paper, we use ego odometry \mathbf{T}_{ol} and transform matrix \mathbf{L}_{lt} extracted from semantic detection module to set object odometry \mathbf{T}_{ot} at the first detected frame.

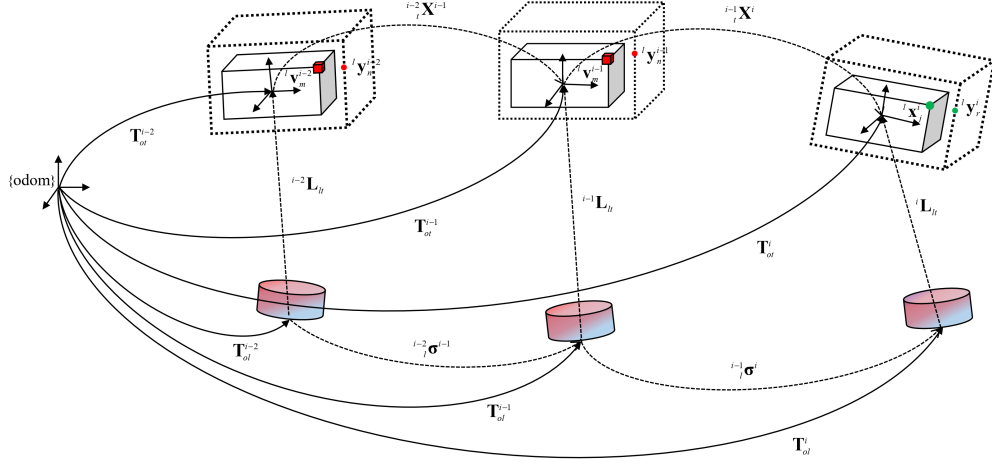


Fig. 4. **Notation and coordinate frames.** Ccolored cylinders denote the Lidar, white cuboids represent a moving object. Dashed cuboids are the result inferred by semantic detection module. Solid lines represent Lidar and object pose in odom coordinate. Dashed lines indicate their motion in body-fixed coordinate. Small red cubes and dots represent voxels whose motion distortion has been eliminated and 3D points obtained by uniform sampling on 3D-BB, respectively. Green dots represent object points in current lidar scan and 3D-BB sampling points without motion distortion.

D. 4D Semantic Object Map

To achieve the reuse of the created map, we suggest maintaining the static consistency map and foreground movable object poses, respectively.

By matching the ground feature $\bar{\chi}_c^i$, background segment $\bar{\psi}_c^i$ and surface feature $\bar{\zeta}_c^i$ with the surrounding point cloud map, ego pose \mathbf{T}_{ol}^i can be corrected to the map coordinate. Then, the long-term static map is obtained by aligning different features into the map coordinate. Readers can read [39] for more map matching and optimization details. Finally, the transform matrix \mathbf{T}_{mo}^i that corrects accumulated error is computed based on ego pose \mathbf{T}_{ol}^i in odom coordinate and corrected pose \mathbf{T}_{ml}^i in map coordinate.

Meanwhile, as shown in Fig.4, object odometry \mathbf{T}_{ot}^i can be expressed as:

$$\mathbf{T}_{ot}^i = \mathbf{T}_{ol}^i \mathbf{L}_{lt}^i \quad (10)$$

We use the transform matrix \mathbf{T}_{mo}^i obtained when creating the static map to get object poses \mathbf{T}_{mt}^i in map coordinate, completing the 4D semantic object map construction.

IV. EXPERIMENT

This section presents experiment details and results for testing the MLO system on the public KITTI dataset. The experiment is divided into three parts: 1) Comparing ego localization accuracy of MLO and A-LOAM system in complex scenes containing high dynamics, unstructured information, and unknown semantics. 2) Evaluating multi-object tracking accuracy and length, verify the advantages of the semantic-geometric joint estimation method. 3) Calculate the average time-consuming of each module and the time-consuming of the multi-object tracking in each frame.

A. Experimental Setup and Error Metrics

The experiment environment of the proposed framework is AMD® Ryzen 7 5800h (8 cores @3.2 GHz), 16GB RAM,

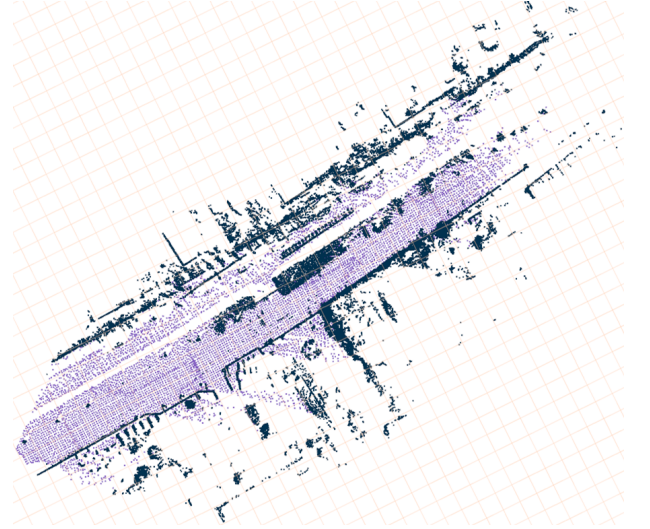


Fig. 5. **Static consistency map in sequence 0926-0013.** Blue point cloud represents background map, and purple point cloud represents the ground. Because semantic objects and static map are maintained separately, there is no "ghosting" problem introduced by object motion in the map.

ROS Melodic, and NVIDIA GeForce RTX 3070. We use absolute trajectory error (ATE) [29], relative rotation error (RRE), and relative translation error (RTE) [10] to evaluate overall accuracy and odometry drift for ego and object localization.

To obtain a smooth and accurate 6-DOF ego pose ground-truth, we use the tightly coupled extended Kalman filter method proposed in [18] to deal with GPS/IMU data in the KITTI-raw dataset. At the same time, combined with high-precision manual object annotation in Lidar coordinate, the ground truth of object pose in map coordinate can also be obtained. In addition, the object detection model proposed by 3DSSD [36] is training based on the KITTI-object dataset. Therefore, experiments in this paper are carried out on a pre-trained model without adjustment.

TABLE I
EVALUATION OF EGO LOCALIZATION ACCURACY UNDER CITY AND RESIDENTIAL SEQUENCES.

Sequence	A-LOAM			MLO(S)			MLO(S+G)		
	ATE[m]	RTE[m/f]	RRE[deg/f]	ATE[m]	RTE[m/f]	RRE[deg/f]	ATE[m]	RTE[m/f]	RRE[deg/f]
City-0926-0011	0.365	0.083	0.111	0.414	0.058	0.080	0.406	0.053	0.072
City-0926-0014	0.441	0.113	0.213	0.236	0.111	0.147	0.249	0.109	0.134
City-0926-0056	0.287	0.124	0.209	18.197	0.508	0.147	0.312	0.121	0.133
City-0926-0059	0.240	0.059	0.134	0.265	0.063	0.104	0.260	0.059	0.098
City-0929-0071	1.634	0.054	0.159	1.623	0.066	0.136	1.620	0.053	0.116
Res-0926-0019	1.809	0.197	0.163	0.406	0.096	0.105	0.383	0.095	0.122
Res-0926-0022	1.922	0.079	0.205	1.944	0.097	0.175	1.851	0.081	0.154
Res-0926-0039	0.559	0.070	0.278	0.474	0.114	0.234	0.482	0.062	0.179
Res-0926-0064	3.519	0.097	0.254	1.833	0.096	0.217	1.646	0.073	0.182
Res-0930-0034	1.770	0.073	0.225	1.612	0.072	0.180	1.745	0.097	0.211
mean	1.255	0.095	0.195	2.700	0.128	0.153	0.895	0.080	0.140

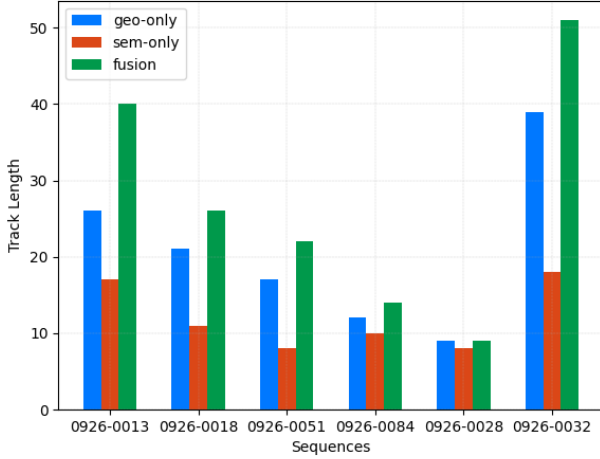


Fig. 6. Average track length of objects in different KITTI-raw sequences.

B. Ego Odometry Localization Accuracy Experiment

The KITTI-raw dataset is used for the localization accuracy experiment with City sequences containing unknown dynamic semantic objects and Residential sequences containing unstructured scenes such as forests.

Table 1 shows the experimental comparison results of A-LOAM, MLO(S) which only considers the semantic rejection method and MLO(S+G), which considers both semantic and geometric methods. Since the KITTI dataset only labels semantic objects within the camera’s field of view, raw lidar scan should be input into the fusion perception module after cutting. Considering the random geometric consistency check algorithm in the MLO system, each sequence is run five times.

It can be seen that MLO proposed in this paper achieves higher localization accuracy than A-LOAM in most sequences. Meanwhile, MLO(S+G) outperforms the other two frameworks on average, RRE and RTE. It is mainly because the introduction of geometric consistency check can filter out invalid high-noise features in the scene. For sequence 0926-0056, a train appears in the near field of view, which cannot be detected by the object detection module, and the two-step pose estimation algorithm increases the proportion of abnormal associations. MLO(S) exhibits apparent trajectory

drift. On the other hand, high-speed trains can still be captured and eliminated by the geometric consistency check algorithm, which ensures the robustness of MLO(S+G) in unknown semantics scenes.

We note that A-LOAM system performs poorly on 3 test sequences. Among them, sequence 0926-0014 contains many near-field moving vehicles in the front part of the dataset. Since A-LOAM does not refine the selection of extracted segment and surface features, features on the vehicle will also participate in localization and mapping work. The other two poor-performing sequences contain long forest and bush scenes, where surface features extracted from the background are not reliable enough. MLO system can effectively avoid this negative impact because of ground smoothness prior.

C. Object Tracking Accuracy and Robustness Experiment

To verify the semantic-geometric joint least squares estimation algorithm (Joint Method) proposed in this paper, we selected eight sequences containing moving objects from City and Road sequences and compared them with object tracking methods using only semantic boxes (Semantic Only) and only geometric point clouds (Geometry Only). Evaluation results of localization accuracy (Table 2) and tracking length (Fig. 6) for objects are shown with the trajectory length greater than five frames. Considering the randomness of the geometric consistency detection algorithm in MLO system, each sequence is run five times.

The localization accuracy of the geometry-only estimation method presents an evident “two-pole” distribution. In the experiment, we found that it can only achieve stable and accurate tracking for objects perceived within 10m. The main reason for this phenomenon is that the lidar points successfully hit on the object will decrease rapidly with the increase of measurement range. When the constraints in some orientations are not complete, it will lead to divergent optimization results.

On the other hand, when an object is in the near field of view, the estimation method based on directly measured point clouds will be more accurate than that of 3D-BB inferred by the semantic detection module. We can obtain this conclusion by comparing semantic and converged geometric tracking results.

TABLE II
EVALUATION OF OBJECT LOCALIZATION ACCURACY UNDER CITY AND ROAD SEQUENCES.

Sequence	object_id	Geometry Only			Semantic Only			Joint Method		
		ATE[m]	RTE[m/m]	RRE[deg/m]	ATE[m]	RTE[m/m]	RRE[deg/m]	ATE[m]	RTE[m/m]	RRE[deg/m]
City-0926-0009	87	0.099	0.099	1.484	-	-	-	0.070	0.089	0.871
	89	0.047	0.057	0.966	0.082	0.083	0.777	0.055	0.063	0.661
City-0926-0013	1	0.049	0.117	1.055	0.096	0.130	0.682	0.101	0.147	0.804
	2	0.085	0.125	2.127	0.145	0.131	0.849	0.121	0.104	0.825
City-0926-0018	5	0.033	0.066	2.345	0.104	0.115	0.748	0.122	0.108	1.715
	6	0.023	0.039	3.145	0.094	0.110	0.863	0.095	0.077	1.430
	11	1.986	1.472	2.975	0.068	0.094	0.915	0.065	0.052	0.922
City-0926-0051	26	2.771	2.345	3.136	0.128	0.095	0.900	0.078	0.070	1.395
	33	0.062	0.079	2.405	0.081	0.106	0.991	0.054	0.098	0.942
City-0926-0084	18	0.120	0.094	2.305	0.145	0.105	0.828	0.081	0.095	0.906
Road-0926-0015	18	0.103	0.091	1.608	0.216	0.184	1.296	0.232	0.141	0.997
	25	2.066	1.992	2.483	-	-	-	0.099	0.136	1.024
	30	-	-	-	0.156	0.137	1.254	0.065	0.096	0.898
Road-0926-0028	3	0.185	0.210	1.398	0.162	0.205	1.058	0.129	0.197	1.808
Road-0926-0032	15	0.182	0.285	1.505	0.147	0.171	0.878	0.182	0.201	0.867
mean		0.588	0.505	2.067	0.125	0.128	0.926	0.103	0.112	1.071

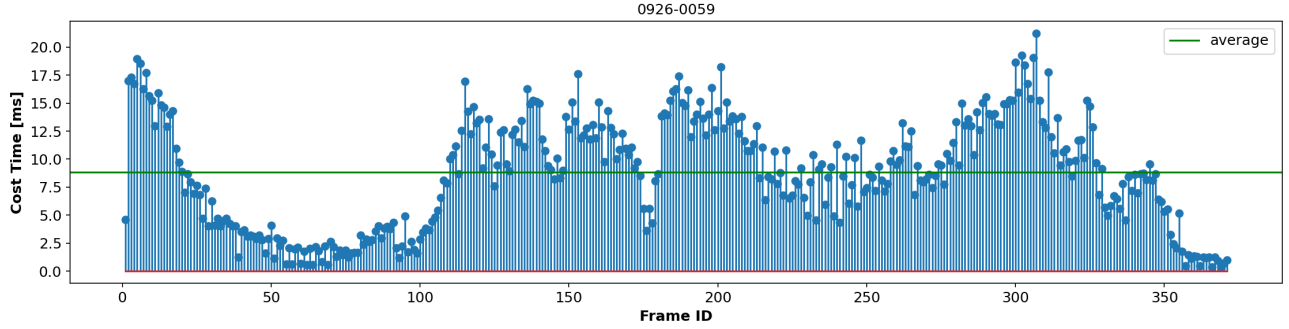


Fig. 7. Time-consuming results of semantic-geometric joint tracking module for sequence 0926-0059 in KITTI-raw dataset.

We hope to use a directly measured object point cloud to improve state estimation accuracy. Meanwhile, we should ensure tracking robustness when the object is moving away from the robot. Therefore, it seems natural to use a joint estimation method with semantic and geometric information. As shown in Table 2, our proposed method does not exhibit evident object trajectory drift and achieves better localization accuracy on all test sequences. Furthermore, it can stably track objects within a field of view of about 25m, and the trajectory length is also longer than the single method.

D. Module Calculation Time

We count the average time-consuming of all functional modules except semantic object detection (which relies on GPU parallel acceleration) in all test sequences. From the results in Table 3, it can be seen that the framework proposed in this paper can run at a real-time frequency which is greater than 10 Hz (perception + localization) if we can guarantee the computational efficiency of the detection module.

Fig.7 presents the time-consuming results of the semantic-geometric joint tracking module (depending on the number of objects processed in real-time) when MLO system runs

in sequences 0926-0059. We can conclude that the time-consuming of our method is always less than 25ms even at the peak time (ten objects are tracked at the same time).

V. CONCLUSIONS AND FUTURE WORK

This paper proposes MLO, a novel multi-object semantic Lidar odometry framework. It only takes lidar scan as input and realizes simultaneous localization, mapping, and tracking of dynamic objects. The performance of MLO is stable and accurate when it works in complex scenes, including unknown semantics and unstructured. Reliable multi-object tracking is achieved through the joint estimation method with both semantic and geometric information. On the other hand, dynamic object-aware visual SLAM technology has developed rapidly. Works such as [11] have verified that the tightly coupled optimization of ego poses, object trajectories, and landmarks based on batch processing can improve the system mapping accuracy. Therefore, exploring the tightly coupled lidar back-end will be a challenging and exciting task.

REFERENCES

- [1] A. Asvadi, P. Girão, P. Peixoto, and U. Nunes, “3d object tracking using rgb and lidar data,” in *2016 IEEE 19th International Conference on Intelligent Transportation Systems (ITSC)*. IEEE, 2016, pp. 1255–1260.

TABLE III
AVERAGE TIME-CONSUMING OF DIFFERENT SYSTEM MODULES UNDER
ALL TEST SEQUENCES.

Module	Operation	Mean [ms]
PERCEPTION	Point Cloud Cutting	10.76
	Geometry Feature Extraction	10.97
	Information Fusion	1.45
LOCALIZATION	Ego Pose Estimation	9.56
	Multi-Object Tracking	3.72
	Object Pose Estimation	0.02
MAPPING	Static Mapping	22.18
	Object Trajectory Correction	0.05

- [2] A. Azim and O. Aycard, "Detection, classification and tracking of moving objects in a 3d environment," in *2012 IEEE Intelligent Vehicles Symposium*. IEEE, 2012, pp. 802–807.
- [3] Baidu, "Apolloauto," <https://github.com/ApolloAuto/apollo>, 2022.
- [4] X. Chen, A. Milioto, E. Palazzolo, P. Giguere, J. Behley, and C. Stachniss, "Suma++: Efficient lidar-based semantic slam," in *2019 IEEE/RSJ International Conference on Intelligent Robots and Systems (IROS)*. IEEE, 2019, pp. 4530–4537.
- [5] Y. Chen and G. Medioni, "Object modelling by registration of multiple range images," *Image and vision computing*, vol. 10, no. 3, pp. 145–155, 1992.
- [6] A. Dewan, T. Caselitz, G. D. Tipaldi, and W. Burgard, "Motion-based detection and tracking in 3d lidar scans," in *2016 IEEE international conference on robotics and automation (ICRA)*. IEEE, 2016, pp. 4508–4513.
- [7] —, "Rigid scene flow for 3d lidar scans," in *2016 IEEE/RSJ International Conference on Intelligent Robots and Systems (IROS)*. IEEE, 2016, pp. 1765–1770.
- [8] F. Ferri, M. Gianni, M. Menna, and F. Pirri, "Dynamic obstacles detection and 3d map updating," in *2015 IEEE/RSJ International Conference on Intelligent Robots and Systems (IROS)*. IEEE, 2015, pp. 5694–5699.
- [9] M. A. Fischler and R. C. Bolles, "Random sample consensus: a paradigm for model fitting with applications to image analysis and automated cartography," *Communications of the ACM*, vol. 24, no. 6, pp. 381–395, 1981.
- [10] A. Geiger, P. Lenz, and R. Urtasun, "Are we ready for autonomous driving? the kitti vision benchmark suite," in *2012 IEEE conference on computer vision and pattern recognition*. IEEE, 2012, pp. 3354–3361.
- [11] M. Henein, J. Zhang, R. Mahony, and V. Ila, "Dynamic slam: the need for speed," in *2020 IEEE International Conference on Robotics and Automation (ICRA)*. IEEE, 2020, pp. 2123–2129.
- [12] C. Jiang, D. P. Paudel, Y. Fougerolle, D. Fofi, and C. Demonceaux, "Static-map and dynamic object reconstruction in outdoor scenes using 3-d motion segmentation," *IEEE Robotics and Automation Letters*, vol. 1, no. 1, pp. 324–331, 2016.
- [13] R. E. Kalman, "A new approach to linear filtering and prediction problems," 1960.
- [14] K. Koide, M. Yokozuka, S. Oishi, and A. Banno, "Voxelized gicp for fast and accurate 3d point cloud registration," in *2021 IEEE International Conference on Robotics and Automation (ICRA)*. IEEE, 2021, pp. 11 054–11 059.
- [15] K. Liu, W. Wang, R. Tharmarasa, and J. Wang, "Dynamic vehicle detection with sparse point clouds based on pe-cpd," *IEEE Transactions on Intelligent Transportation Systems*, vol. 20, no. 5, pp. 1964–1977, 2018.
- [16] K. Madsen, H. B. Nielsen, and O. Tingleff, "Methods for non-linear least squares problems," 2004.
- [17] A. Milioto, I. Vizzo, J. Behley, and C. Stachniss, "Rangenet++: Fast and accurate lidar semantic segmentation," in *2019 IEEE/RSJ International Conference on Intelligent Robots and Systems (IROS)*. IEEE, 2019, pp. 4213–4220.
- [18] T. Moore and D. Stouch, "A generalized extended kalman filter implementation for the robot operating system," in *Intelligent autonomous systems 13*. Springer, 2016, pp. 335–348.
- [19] F. Moosmann and T. Fraichard, "Motion estimation from range images in dynamic outdoor scenes," in *2010 IEEE International Conference on Robotics and Automation*. IEEE, 2010, pp. 142–147.
- [20] F. Moosmann and C. Stiller, "Joint self-localization and tracking of generic objects in 3d range data," in *2013 IEEE International Conference on Robotics and Automation*. IEEE, 2013, pp. 1146–1152.
- [21] R. Mur-Artal, J. M. M. Montiel, and J. D. Tardos, "Orb-slam: a versatile and accurate monocular slam system," *IEEE transactions on robotics*, vol. 31, no. 5, pp. 1147–1163, 2015.
- [22] S. Park, T. Schöps, and M. Pollefeys, "Illumination change robustness in direct visual slam," in *2017 IEEE international conference on robotics and automation (ICRA)*. IEEE, 2017, pp. 4523–4530.
- [23] F. Pomerleau, P. Krüsi, F. Colas, P. Furgale, and R. Siegwart, "Long-term 3d map maintenance in dynamic environments," in *2014 IEEE International Conference on Robotics and Automation (ICRA)*. IEEE, 2014, pp. 3712–3719.
- [24] A. Pumarola, A. Vakhitov, A. Agudo, A. Sanfeliu, and F. Moreno-Noguer, "Pl-slam: Real-time monocular visual slam with points and lines," in *2017 IEEE international conference on robotics and automation (ICRA)*. IEEE, 2017, pp. 4503–4508.
- [25] Y. Qiu, C. Wang, W. Wang, M. Henein, and S. Scherer, "Airdos: Dynamic slam benefits from articulated objects," *arXiv preprint arXiv:2109.09903*, 2021.
- [26] P. Ruchti and W. Burgard, "Mapping with dynamic-object probabilities calculated from single 3d range scans," in *2018 IEEE International Conference on Robotics and Automation (ICRA)*. IEEE, 2018, pp. 6331–6336.
- [27] T. Shan and B. Englot, "Lego-loam: Lightweight and ground-optimized lidar odometry and mapping on variable terrain," in *2018 IEEE/RSJ International Conference on Intelligent Robots and Systems (IROS)*. IEEE, 2018, pp. 4758–4765.
- [28] S. Shi, X. Wang, and H. Li, "Pointcrnn: 3d object proposal generation and detection from point cloud," in *Proceedings of the IEEE/CVF conference on computer vision and pattern recognition*, 2019, pp. 770–779.
- [29] J. Sturm, N. Engelhard, F. Endres, W. Burgard, and D. Cremers, "A benchmark for the evaluation of rgb-d slam systems," in *2012 IEEE/RSJ international conference on intelligent robots and systems*. IEEE, 2012, pp. 573–580.
- [30] D. Sun, X. Yang, M.-Y. Liu, and J. Kautz, "Pwc-net: Cnns for optical flow using pyramid, warping, and cost volume," in *Proceedings of the IEEE conference on computer vision and pattern recognition*, 2018, pp. 8934–8943.
- [31] B. Triggs, P. F. McLauchlan, R. I. Hartley, and A. W. Fitzgibbon, "Bundle adjustment—a modern synthesis," in *International workshop on vision algorithms*. Springer, 1999, pp. 298–372.
- [32] C.-C. Wang, C. Thorpe, and S. Thrun, "Online simultaneous localization and mapping with detection and tracking of moving objects: Theory and results from a ground vehicle in crowded urban areas," in *2003 IEEE International Conference on Robotics and Automation (Cat. No. 03CH37422)*, vol. 1. IEEE, 2003, pp. 842–849.
- [33] C.-C. Wang, C. Thorpe, S. Thrun, M. Hebert, and H. Durrant-Whyte, "Simultaneous localization, mapping and moving object tracking," *The International Journal of Robotics Research*, vol. 26, no. 9, pp. 889–916, 2007.
- [34] H. Wang, B. Wang, B. Liu, X. Meng, and G. Yang, "Pedestrian recognition and tracking using 3d lidar for autonomous vehicle," *Robotics and Autonomous Systems*, vol. 88, pp. 71–78, 2017.
- [35] X. Weng, J. Wang, D. Held, and K. Kitani, "3d multi-object tracking: A baseline and new evaluation metrics," in *2020 IEEE/RSJ International Conference on Intelligent Robots and Systems (IROS)*. IEEE, 2020, pp. 10 359–10 366.
- [36] Z. Yang, Y. Sun, S. Liu, and J. Jia, "3dssd: Point-based 3d single stage object detector," in *Proceedings of the IEEE/CVF conference on computer vision and pattern recognition*, 2020, pp. 11 040–11 048.
- [37] D. Yoon, T. Tang, and T. Barfoot, "Mapless online detection of dynamic objects in 3d lidar," in *2019 16th Conference on Computer and Robot Vision (CRV)*. IEEE, 2019, pp. 113–120.
- [38] D. Zermas, I. Izzat, and N. Papanikolopoulos, "Fast segmentation of 3d point clouds: A paradigm on lidar data for autonomous vehicle applications," in *2017 IEEE International Conference on Robotics and Automation (ICRA)*. IEEE, 2017, pp. 5067–5073.
- [39] J. Zhang and S. Singh, "Loam: Lidar odometry and mapping in real-time," in *Robotics: Science and Systems*, vol. 2, no. 9. Berkeley, CA, 2014, pp. 1–9.
- [40] J. Zhang, M. Henein, R. Mahony, and V. Ila, "Vdo-slam: a visual dynamic object-aware slam system," *arXiv preprint arXiv:2005.11052*, 2020.